


Article

Design and Analysis of Active Speed-Limit Mechanism for Large-Scale Spatial Solar Array

Shuli Yang ^{1,*}, Limin Shao ¹, Lin Li ¹, Mutian Li ¹ and Yunshuai Chen ² ¹ Beijing Institute of Spacecraft System Engineering, China Academy of Space Technology, Beijing 100094, China² School of Mechanical and Precision Instrument Engineering, Xi'an University of Technology, Xi'an 710048, China

* Correspondence: jelly_5251@163.com

Abstract: The multidimensional deployment of large-scale spatial solar arrays has been the basis for high-power advanced spacecraft and a symbol of the leaps forward in aerospace technology. Activated and passive drives have often been used in combination to implement the driving mechanism of large-scale solar arrays, which can reduce the impact of the deployment and locking process. For the first time, a novel active speed-limit mechanism was introduced into the two-dimensional secondary deployable drive system of a large-scale spatial solar array, achieving a balance between large deployable driving torque and small locking impact load. A highly integrated and lightweight drive system has been designed, integrating motor drive, gear drive, and adaptive torque limiting device to achieve adaptive control of the deployment torque of the solar array. A dynamic simulation system for the entire process of a large-scale spatial solar array based on the Kane method and ADAMS model has been established. A two-dimensional secondary deployable motion control law for a large-scale solar array using an active speed-limit mechanism has been established, and the dynamic characteristic parameters of the active speed-limit driving mechanism have been determined, such as driving torque, driving mode, and driving speed. The results can be used to guide the design of the deployable driving mechanism for large-scale spatial solar arrays.

Keywords: large-scale spatial solar array; active speed-limit mechanism; dynamic analysis; torque limiter



Citation: Yang, S.; Shao, L.; Li, L.; Li, M.; Chen, Y. Design and Analysis of Active Speed-Limit Mechanism for Large-Scale Spatial Solar Array. *Coatings* **2023**, *13*, 1351. <https://doi.org/10.3390/coatings13081351>

Academic Editor: Alessandro Latini

Received: 7 July 2023

Revised: 24 July 2023

Accepted: 27 July 2023

Published: 1 August 2023



Copyright: © 2023 by the authors. Licensee MDPI, Basel, Switzerland. This article is an open access article distributed under the terms and conditions of the Creative Commons Attribution (CC BY) license (<https://creativecommons.org/licenses/by/4.0/>).

1. Introduction

The solar array is the primary device of power supply for spacecraft, and the deployable reliability of the solar array directly determines the mission success of the spacecraft [1]. The deployment of the solar array is primarily a passive process based on elastic elements [2,3]. Generally, the solar array needs to be constantly accelerated during the deployable process, and when it deploys at the specified position, the kinetic energy of the solar array is converted into a driving torque sufficient to overcome the locking resistance of the deploying mechanism in order to ensure the reliable locking of the solar array and achieve the predetermined deployment stiffness [4]. However, this deployable process could significantly impact the spacecraft or Solar Array Drive Assembly (hereafter referred to as SADA), leading to satellite attitude being out of control or SADA damage, in severe cases, leading to mission failure [5]. Therefore, for solar arrays, especially large ones, considering the relationship between deployable reliability and reduction of deployment impact is critical to ensure the reliable operation of the spacecraft in orbit [6–9].

If the deployable mechanism is driven passively, the initial pretightening torque of the spring in each hinge is reasonably distributed by analyzing the driving torque required for the full deployment of the large solar array, which minimizes the impact caused by residual energy after deployment. However, to ensure the reliability of on-orbit deployment and locking, the design specification of the solar array requires that the static moment margin must be greater than 1 in the most extreme environment during the whole process, from stowed configuration to full deployment [10]. Therefore, the impact load can only partially

be reduced to a reasonable level by lowering the initial driving torque of the spring. If the passive drive and passive deceleration modes are adopted, the viscous damper is installed at the root of the solar array [11]. This damper is installed to reduce the deploying speed and the impact load by dissipating the mechanical energy of the system during the deploying process. However, the drag moment produced by the viscous damper negatively influences the deployable reliability. In addition, for large solar arrays that require large driving torque, the bearing capacity of existing dampers may be exceeded, which may lead to the failure of the damping effect or force the use of high-capacity dampers with higher volume and weight costs [12,13]. If the solar array's deployment mode is changed from passive to active deployment, during the deployment process of the solar array, the electronic system controls the motor's speed to ensure a reasonable deployment speed. However, this scheme requires special control equipment, including software and hardware circuits and supporting external interfaces. This will significantly increase the complexity of the deployment system, and reduce system reliability to some extent [14–17].

The combination of traditional coil spring drive and viscous damper cannot effectively solve the unique contradiction between the large driving torque and small locking impact load of a large-sized multi-panel solar array. Therefore, for the first time, an active speed-limit mechanism is introduced to replace the viscous damper, achieving a balance between the large driving torque and the small locking impact load. The designed adaptive speed-limit mechanism cleverly combines motor drive, gear transmission, and mechanical torque limiting devices, achieving predetermined functional performance under limited space and weight constraints. For the first time, a mathematical simulation system covering the entire process, from torque limiter action to solar array deployment, has been established, extracting key design parameters, providing a method for evaluating the effectiveness of adaptive speed-limit mechanisms, and conducting subsequent detailed parameter optimization designs that can be quickly iterated.

Considering the abovementioned methods comprehensively, an active speed-limit driving mechanism suitable for use with large-scale spatial solar array is proposed. While adopting a passive driving mechanism with low impact and small driving torque, the adaptive active speed-limit driving mechanism (motor–reducer assembly) can be used to provide resistance torque or to drive torque (resistance torque is generated when the expansion speed of the solar array increases too quickly, and driving torque is provided when the expansion torque of the hinge between panels is insufficient). The motor drive of this mechanism only needs a regulated DC power supply, and the control of driving torque is entirely dependent on the self-adaptation of the mechanism without complicated hardware and software control equipment. Solar array deployment becomes stable, which provides reliability for large solar arrays and effectively reduces locking impacts. Based on the novel design, it is necessary to simulate and calculate the impact on the deployable dynamics of the entire solar array after installing this mechanism. Therefore, the Kane and ADAMS methods have been used to simulate the deployable dynamic process of a large-scale solar array based on the active speed-limit mechanism, and the motion rules of the solar array have been established. Dynamic characteristic parameters (such as the driving torque, driving mode, and driving speed of the active speed-limit mechanism) have been obtained. The abovementioned results can be used to guide the detailed design and application of the active speed-limit mechanism for large-scale spatial solar arrays.

2. The General Plan of a Large-Scale Spatial Solar Array

In this study, we take a large-scale spatial solar array with two-dimensional deployment as an example to design the active speed limit [18,19]. Its composition diagram is shown in Figure 1, including the following components: six solar panels (including solar cell circuits, interboard, and intraboard cables); one yoke; one set of release devices; one set of passive driving mechanisms based on the spring system; and one set of active speed-limit driving mechanisms.

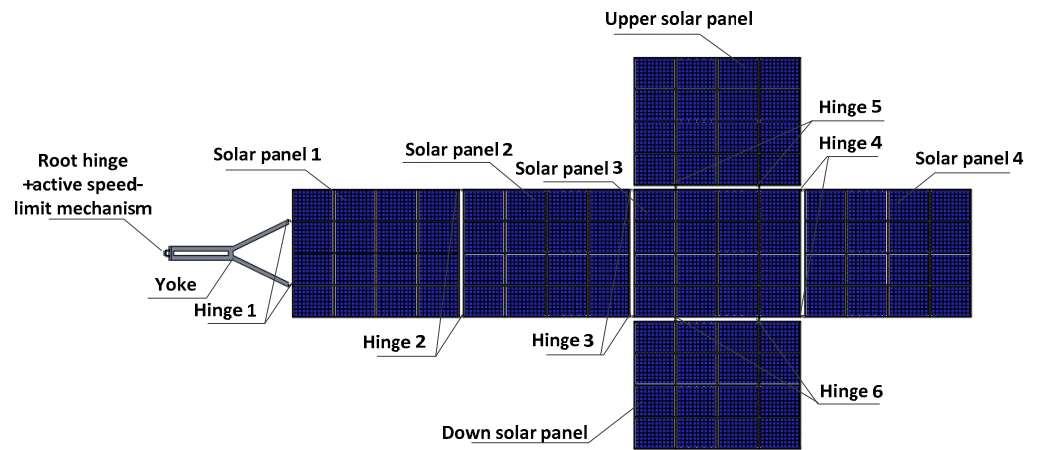


Figure 1. Schematic diagram of the composition of a two-dimensional secondary expansion solar array.

The deployment process of the two-dimensional deployable solar array is shown in Figure 2. ① In the launch phase of the satellite, the solar array is folded and stowed against the sidewall of the satellite. ② When the satellite arrives at the transfer orbit, part of the release mechanism is unlocked, the outer panel of the solar array is expanded to 90° and locked, and the remaining five solar panels stay in a stowed configuration. ③ When the satellite reaches the quasi-synchronous orbit, the remaining release mechanisms are unlocked, the remaining yoke and other solar panels begin to unfold, and the outer solar panel is unlocked and unfolded together with other solar panels and locked again. ④ When the locking in one-dimensional direction is about to start, the side release mechanism is triggered, and the upper and lower solar panels begin to expand. ⑤ The entire solar array extends and locks into a plane.

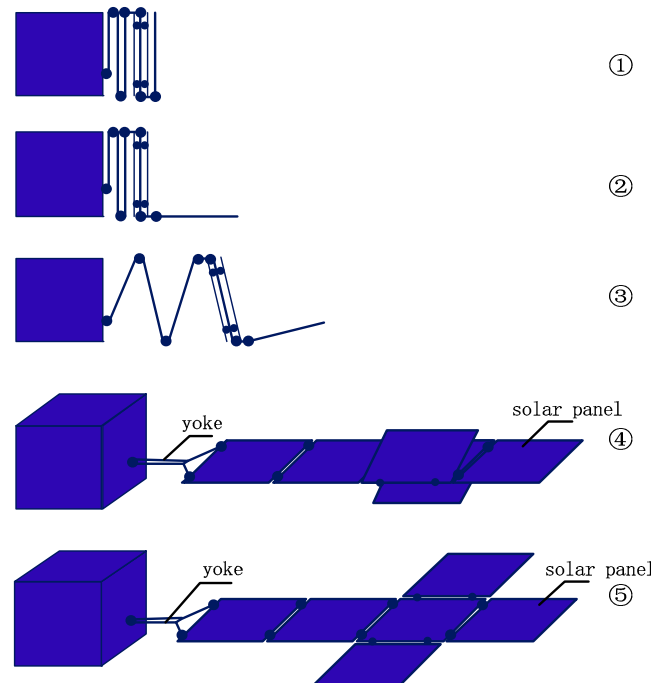


Figure 2. Schematic diagram of the deployment process of a two-dimensional secondary deployment solar array.

The technical indicators of the active speed-limit driving mechanism are as follows:

- (1) Voltage of motor: 28~31 V DC;
- (2) Speed of output shaft: 1~3°/s;

- (3) Rated output torque: 50 N.m, withstanding load of 95 N.m instantaneously;
- (4) When the load exceeds 95 N.m, the torque limiter works to protect the motor from overload;
- (5) Working temperature: $-20 \sim 75$ °C;
- (6) Weight: less than 1.0 kg.

3. Design of an Active Speed-Limit Driving Mechanism

3.1. Principle of an Active Speed-Limit Driving Mechanism

The installation of the active speed-limit driving mechanism has strict volume requirements and needs to ensure sufficient strength and stiffness [20,21]. This paper proposes an integrated speed-limit mechanism based on the motor assembly, torque limiter, and reduction drive chain. The active speed-limit driving mechanism mainly consists of a motor, torque limiter, planetary gear train, and harmonic reducer. The output shaft of the harmonic reducer is connected to the root hinge of the solar array. Its transmission schematic diagram is shown in Figure 3, by which transmission deceleration and torque protection can be realized at the same time.

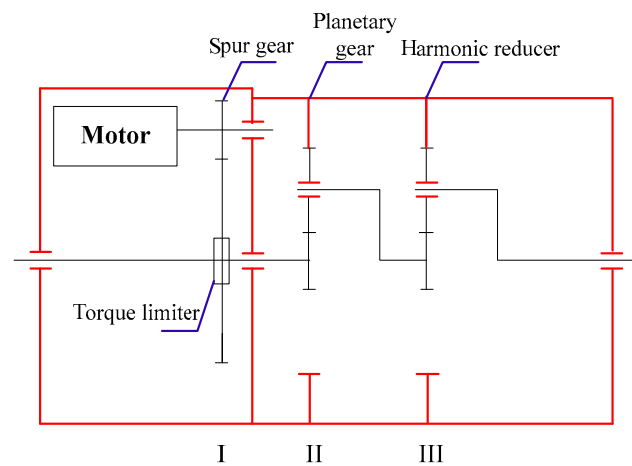


Figure 3. Transmission schematic diagram (in this picture, I represents first-level deceleration, II represents second-level deceleration, and III represents third-level deceleration).

To satisfy the requirements of integration and being lightweight, the configuration layout of the active speed-limit driving mechanism has been optimized by distributing the parameters in a reasonable way and designing the transmission mode to minimize its volume, reduce the number of parts, and improve reliability. This configuration is shown in Figure 4.

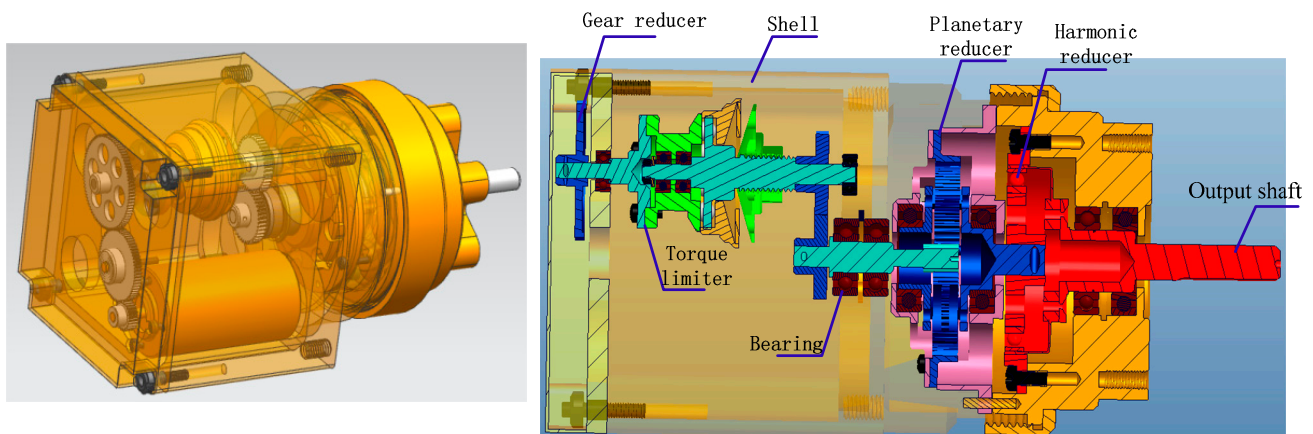


Figure 4. Configuration of the active speed-limit driving mechanism (left) and sectional view of the active speed-limit driving mechanism (right).

3.2. Torque Limiter Design

The torque limiter is the core component of the active speed-limit driving mechanism. Its primary function is to protect the transmission system through clutch action and adapt to overload that may occur during the operation of the active speed-limit driving mechanism or protect the safety of the transmission system when there is a severe impact [22].

3.2.1. Principle of the Steel Ball-Type Torque Limiter

The torque limiter generally has four types: shear pin type, friction plate type, spring tooth embedded type, and spring steel ball type. The spring steel ball-type torque limiter has high sensitivity to torque change, with the characteristics of accurate action, high precision, and reliable operation. It can effectively limit the output torque of the speed-limit mechanism, while ensuring that it can be disconnected in time in the case of overload, protecting the parts of the speed-limit mechanism, and automatically resuming work. It is entirely applicable to the speed-limit driving mechanism. The working principle of the steel ball-type torque limiter is that when the load on the output shaft is small, the disc spring will not produce compression deformation, the steel ball will not slip, and it will contact the tooth grooves at the driving part and the driven part. The role of the torque limiter is equivalent to coupling; when the required torque exceeds the set value (limit torque) due to load vibration, overload, or mechanical failure, the disc spring is compressed, and the steel ball slips on the arc groove, leaving the driving part (the driven shaft stops rotating, limiting the torque transmitted by the transmission system). When the overload condition disappears, the coupling is recovered, which prevents mechanical damage and overload damage to the drive components. The torque limiter is set at the front stage of the planetary reducer and the rear stage of the spur gear transmission, which is conducive to reducing the slip torque and weight; it also prevents the input speed of the torque limiter from being too high, in order to reduce wear. When the active speed-limit driving mechanism bears a load of 95 N.m, the load on the output part of the torque limiter is 0.076 N.m. Considering that the slip torque must be greater than 30% of the maximum working torque, the slip torque is 0.1 N.m. The design of the torque limiter is shown in Figure 5.

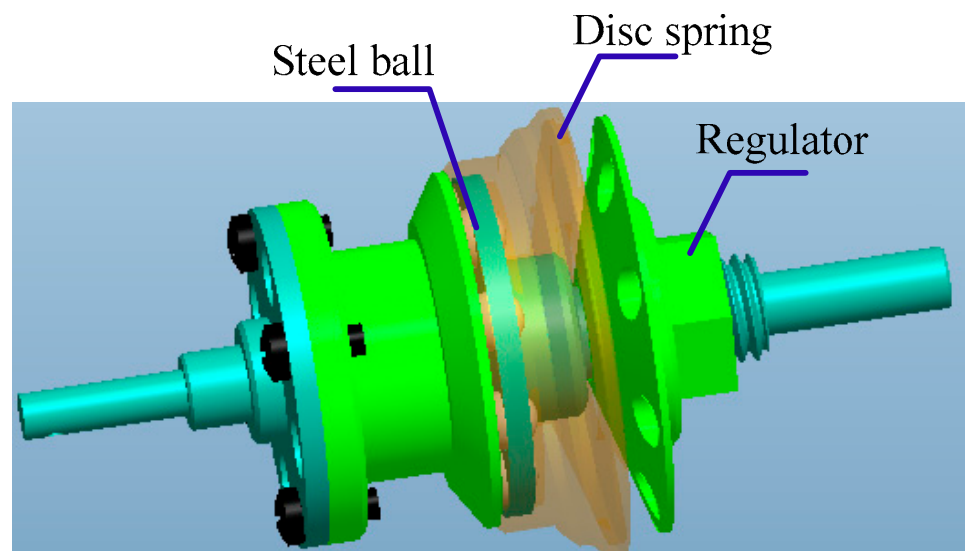


Figure 5. Design of torque limiter.

3.2.2. Parameter Analysis

The key to the design of the steel ball torque limiter is to determine the relationship between the compression force of the disc spring acting on the steel ball and the limiting torque of the limiter, as well as selecting the appropriate contact strength formula to check the contact stress between the steel ball and the tooth socket.

The limit torque transmitted by the limiter is predetermined by design. The key to its calculation is to determine the relationship between the compression force and torque of the disc spring acting on the steel ball. The steel ball is taken as a research object for mechanical analysis based on the limiter’s principle of operation. As shown in Figure 6, when the driven shaft rotates, the steel ball is subjected to four kinds of forces in the tooth socket at the input part (connecting flange), including the circumferential force F_y (the component of the reaction force from the tooth socket at the driven part to the steel ball), the positive pressure in the normal direction of the tooth socket surface F_R , the friction between the steel ball and the tooth socket surface F_f , and the axial pressure of the disc spring on a single steel ball P_1 . Before the steel ball is separated from the tooth socket, its expressions are as follows

$$P_1 = F_R \times \cos \alpha - F_f \times \sin \alpha \tag{1}$$

$$P_1 = P_z / Z \tag{2}$$

$$F_y = F_R \times \sin \alpha + F_f \times \cos \alpha \tag{3}$$

$$F_y = \mu \times F_R \tag{4}$$

where P is the load of a single disc spring (N); P_z is the load of disc spring set (N), if n disc springs are combined, then $P_z = nP$; Z is the number of steel balls; F_y is the circumferential force transmitted by a single steel ball (N); F_f is the sliding friction force between the tooth socket and the steel ball (N); α is the contact angle; μ is the friction coefficient of the working surface, $\mu = \tan \rho$ (ρ is the friction angle, as $5 \sim 6^\circ$).

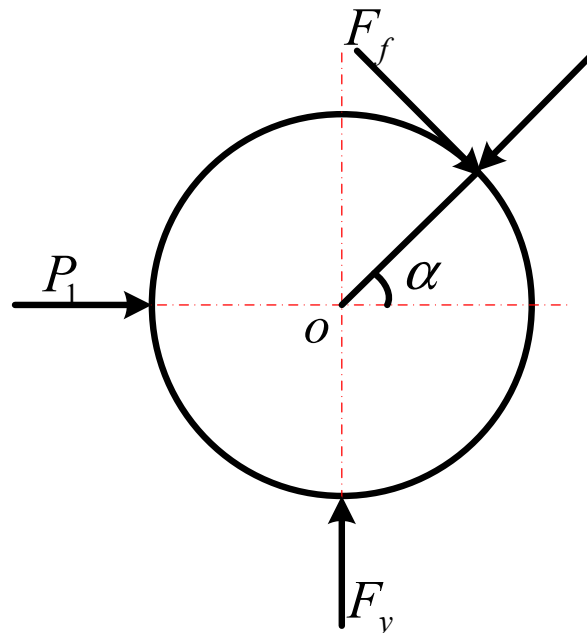


Figure 6. Stress diagram of single steel ball.

Solve Equations (1), (3) and (4) and sort them out

$$P_1 = \tan^{-1}(\alpha + \rho) \times F_y \tag{5}$$

$$F_R = \frac{\cos \rho}{\sin(\alpha + \rho)} \times F_y \tag{6}$$

If the limiting torque transmitted by the limiter is T_j , and the diameter of the dividing circle of steel ball is D_m , then

$$F_y = \frac{2T_j}{D_m \times Z} \tag{7}$$

$$P_1 = \frac{2T_j}{D_m \times Z} \times \tan^{-1}(\alpha + \rho) \tag{8}$$

In the active speed-limit driving mechanism, $T_j = 0.1$ N.m, $D_m = 16$ mm, and the number of steel balls is $Z = 8$, so a single steel ball $F_y = 1.56$ N. The axial pressure of the disc spring on a single steel ball is $P_1 = 1.29$ N. The load to be provided by the disc spring is $P_z = 10$ N.

3.2.3. Strength Check

The contact surface between the steel ball and tooth socket is taken for a fatigue strength check. If two profiled surfaces come into contact without force, the initial contact will be primarily line and point. Hertz stress is generated when the steel ball and the arc surface of the tooth socket extrude each other. This is similar to the contact between the ball and the concave spherical surface. The contact area is generally elliptical or circular. The profile of the connection between the steel ball and the tooth socket is shown in Figure 7, where H is the depth of the tooth socket. The tooth socket’s modulus and Poisson’s ratio are μ_1, E_1 , and the elastic modulus and Poisson’s ratio of the steel ball are μ_2, E_2 .

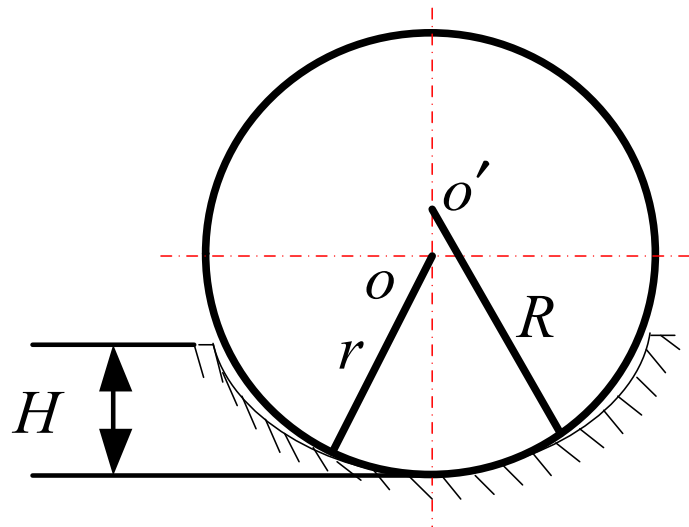


Figure 7. Profile of contact between steel ball and circular tooth socket.

According to the knowledge of elasticity, when the contact area is elliptical, the maximum contact stress is as follows

$$\sigma_{Hmax} = \frac{3F}{2\pi} \left[\frac{4(R - r)}{3\pi \times F \times (k_1 + k_2) \times R \times r} \right]^{\frac{2}{3}} \tag{9}$$

where: F is the normal load at the contact (N), $F = \frac{\cos \rho}{\sin(\alpha + \rho)} \times F_y$; $k_1 = \frac{1 - \mu_1^2}{E_1}$, $k_2 = \frac{1 - \mu_2^2}{E_2}$. R is the radius of curvature of the tooth socket; r is the radius of the steel ball.

Strength check: $\sigma_{Hmax} \leq \sigma_{HP}$, σ_{HP} is the allowable contact stress, which can be calculated according to σ_{lim}/S .

In the active speed-limit driving mechanism, $\mu_1 = \mu_2 = 0.45$, $E_1 = E_2 = 2 \times 10^{11}$ Pa, $R = 4.2$ mm, $r = 4$ mm. Then, the normal load at the contact point $F = 2.03$ N; the maximum contact stress σ_{Hmax} is 7.089×10^8 Pa, far less than the allowable contact stress σ_{HP} of 6.3×10^{10} Pa, so the strength meets the requirements.

3.3. Parameter Design

Parameter values of the active speed-limit driving mechanism are shown in Table 1. Weight estimation of the active speed-limit driving mechanism is shown in Table 2.

Table 1. Parameter values of DC motor + gearbox + planetary reduction + harmonic reduction for the scheme.

Parameter	Unit	Rated State	Maximum Torque Output State
The angular speed of output shaft of active speed-limit driving mechanism	°/s	3	3
Output shaft speed of active speed-limit driving mechanism	rpm	0.5	0.5
The output torque of active speed-limit driving mechanism	N.m	50 (rated torque)	95 (maximum)
Third stage harmonic reduction ratio	-	160	160
The inner diameter of harmonic flexspline	mm	50	50
Input speed of harmonic	rpm	80	80
Resistance torque of harmonic and output shaft system	N.m	0.05	0.05
Starting torque of the harmonic reducer	N.m	0.01	0.01
Drive efficiency of harmonic	-	50%	50%
Second stage planetary reduction ratio	-	25	25
Input speed of planetary	rpm	2000	2000
Resistance torque of planetary and output shaft system	N.m	0.05	0.05
Starting torque of the planetary reducer	N.m	0.01	0.01
Transmission efficiency of planetary	-	80%	80%
First stage spur gear reduction ratio	-	3	3
Input speed of gear	rpm	6000	6000
Resistance torque of gear and output shaft system	N.m	0.0	0.0
Starting torque of gear	N.m	0.01	0.01
Transmission efficiency of gear	/	50%	50%
Output torque at planetary part	N.m	0.6705	1.270
Output torque at gear part	N.m	0.046	0.075
Output torque at motor part	N.m	0.1	0.15

Table 2. Weight estimation of active speed-limit driving mechanism.

S/N	Component	Weight
1	motor	146 g
2	shell, shafting and support	450 g
3	reducer assembly	253 g
4	total	849 g

4. Dynamics Modeling of a Large-Scale Spatial Solar Array Based on the Kane Method

To determine whether the space deployable mechanism can be stably and reliably deployed and whether the dynamic characteristics of the entire moving process can meet the optimal design requirements, it is necessary to conduct dynamic modeling of the deployment mechanism of the solar array to master the dynamic characteristics, such as the speed, acceleration, deployment time, and geometric configuration of the solar array deployment [23,24].

4.1. Establishment of the Analysis Model

The Kane method has the advantages of both vector and analytical mechanics [25–28]. Nevertheless, it has yet to have a universal form of dynamic equation suitable for any multirigid body system, and each specific multirigid body system must be specifically treated.

For the two-dimensional solar array, the drive module only has the active speed-limiting function for the parts, including the yoke, inner panel, inner-middle panel, outer-middle panel, and outer panel; thus, the dynamic modeling is only conducted for the one-dimensional direction.

To facilitate the analysis and modeling, the following assumptions are made for the mechanical model of solar array deployment:

- (1) Both the yoke and the panels are rigid elements that do not deform in the whole moving process;

- (2) Each panel is a homogeneous element, and its center of mass is in the center of each panel;
- (3) The energy consumption of each hinge during the movement is ignored; that is, the friction in each motion pair is ignored;
- (4) In the analysis process, the torque is specified as positive counterclockwise and negative clockwise, and all forces are positive vertically and horizontally.

4.2. Establishment of the Analysis Model

The simplified model of the deployment process is shown in Figure 8. The Cartesian coordinate system is established and the unit vectors in three directions are defined as $e_1^{(0)}, e_2^{(0)}, e_3^{(0)}$. The angle of the root hinge θ is selected as the generalized coordinate.

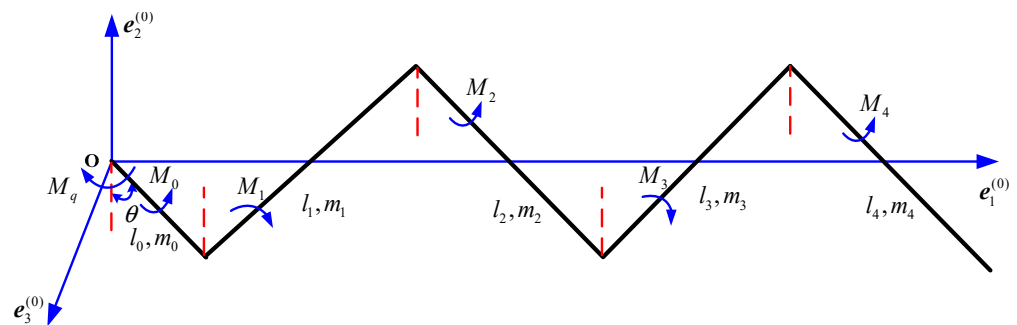


Figure 8. Schematic diagram of coordinate system selection and force of solar array.

4.3. Kinematic Analysis of Solar Array Deployment

Each component’s displacement, velocity, and acceleration are expressed as functions of generalized coordinates. In the case shown in Figure 8, external forces include inertial force and inertial moment. To obtain the inertial force and moment of components, it is necessary to determine the relationship between the position, velocity, and acceleration of the center of mass of each element and the generalized coordinates. Suppose the centroid displacement and angular displacement vectors of each component are $L_i, \theta_i, (i = 0,1,2,3,4)$, respectively. The centroid velocity and angular velocity vectors for each member are $V_{ci}, \omega_i, (i = 0,1,2,3,4)$, respectively. The acceleration vector and angular acceleration vector of each member are $a_{ci}, \varepsilon_i, (i = 0,1,2,3,4)$, respectively, and the moment of inertia of each member around the center of mass is $J_i, (i = 0,1,2,3,4)$.

4.3.1. Position, Velocity and Acceleration of the Center of Mass of Each Pane

The position of the center of mass is represented by a vector L_i

$$\left\{ \begin{array}{l} L_0 = l_0/2 \times \sin \theta \times e_1^{(0)} - l_0/2 \times \cos \theta \times e_2^{(0)} \\ \theta_0 = \theta \times e_3^{(0)} \\ L_1 = (l_0 + l_1/2) \times \sin \theta \times e_1^{(0)} + (l_1/2 - l_0) \times \cos \theta \times e_2^{(0)} \\ \theta_1 = -\theta \times e_3^{(0)} \\ L_2 = (l_0 + l_1 + l_2/2) \times \sin \theta \times e_1^{(0)} + (l_1 - l_0 - l_2/2) \times \cos \theta \times e_2^{(0)} \\ \theta_2 = \theta \times e_3^{(0)} \\ L_3 = (l_0 + l_1 + l_2 + l_3/2) \times \sin \theta \times e_1^{(0)} + (l_1 - l_0 - l_2 - l_3/2) \times \cos \theta \times e_2^{(0)} \\ \theta_3 = -\theta \times e_3^{(0)} \\ L_4 = (l_0 + l_1 + l_2 + l_3 + l_4/2) \times \sin \theta \times e_1^{(0)} + (l_1 - l_0 - l_2 - l_3 - l_4/2) \times \cos \theta \times e_2^{(0)} \\ \theta_4 = -\theta \times e_3^{(0)} \end{array} \right. \quad (10)$$

Let the derivative of generalized coordinates with respect to time be generalized velocity: $u = \dot{\theta}$; according to Equation (10), the centroid velocity, angular velocity, centroid accel-

eration, and angular acceleration of each component are shown in Equations (11) and (12), respectively, and they are converted into expressions for generalized coordinates and generalized velocity.

$$\begin{cases} V_{ci} = \frac{dL_i}{dt} \\ \omega_i = \frac{d\theta_i}{dt} \end{cases} \quad (i = 0, 1, 2, 3, 4) \tag{11}$$

$$\begin{cases} a_{ci} = \frac{d^2L_i}{dt^2} = \frac{dV_{ci}}{dt} \\ \varepsilon_i = \frac{d^2\theta_i}{dt^2} = \frac{d\omega_i}{dt} \end{cases} \quad (i = 0, 1, 2, 3, 4) \tag{12}$$

4.3.2. Main Force and Inertial Force in the Deployment Process of the Solar Array

The moment of each component is $M_i, (i = 0, 1, 2, 3, 4)$, respectively, and then the active moment is

$$\begin{cases} M_0 = (-M_q + M_0) \times e_3^{(0)} \\ M_1 = -M_1 \times e_3^{(0)} \\ M_2 = M_2 \times e_3^{(0)} \\ M_3 = -M_3 \times e_3^{(0)} \\ M_4 = -M_4 \times e_3^{(0)} \end{cases} \tag{13}$$

where M_q is the torque of the active speed-limit driving mechanism; the driving torque M_0, M_1, M_2, M_3 is provided by each hinge point of the solar array. Assuming that the spring is linear, the driving forces generated by the root hinge and the panel hinge are respectively expressed as

$$\begin{cases} T_{s0} = T_{s0}^d + K_{s0} \times (\frac{\pi}{2} - \theta) \\ T_{si} = T_{si}^d + 2K_{si} \times (\frac{\pi}{2} - \theta) \end{cases} \quad i = 1, 2, 3, 4 \tag{14}$$

In Equation (14), T_s^d represents the remaining torque value of ($\theta = \frac{\pi}{2}$) of the spring at the end of deployment; K_s is the spring constant. It should be noted that T_s^d and K_s are for hinge pairs. In Equation (14), the coefficient 2.0 takes into account that the torsional angle change of the hinge between panels is 2θ .

In addition to the active torque generated by the spring and the active speed-limiting mechanism, the resistance torque is generated by cable, tension rope, hinge friction, and other factors in each hinge pair. The total resistance moment on the rotation axis can be simplified, as shown in Equation (15).

$$\begin{cases} T_{r0} = T_{r0}^d + K_{r0} \times (\frac{\pi}{2} - \theta) \\ T_{ri} = T_{ri}^d + 2K_{ri} \times (\frac{\pi}{2} - \theta) \end{cases} \quad i = 1, 2, 3, 4 \tag{15}$$

In Equation (15), T_r^d is the total resistance moment at the end of deployment. K_r is equivalent to a "spring constant." It is assumed that the resistance torque increases gradually according to the linear law, which is consistent with the actual situation.

Therefore, the driving torque $M_i, (i = 0, 1, 2, 3, 4)$ provided by each hinge pair of the solar array can be expressed as

$$M_i = T_{si} + T_{ri}, i = 0, 1, 2, 3, 4 \tag{16}$$

The moment of inertia is

$$F_i^* = -m_i \times a_{ci}, M_i^* = -J_i \times \varepsilon_i (i = 0, 1, 2, 3, 4) \tag{17}$$

4.3.3. Generalized Active Force and Generalized Inertial Force

The active force and inertial force are transferred to generalized coordinates. First, the partial velocity is calculated, which is the partial derivative of each point's velocity and the component's angular velocity to the generalized velocity (also called the partial velocity).

A conversion matrix is formed and multiplied by the force vector to obtain the generalized force. The conversion matrix of the force is as follows.

$$U_F = \left[\frac{\partial V_{c0}}{\partial u}, \frac{\partial V_{c1}}{\partial u}, \frac{\partial V_{c2}}{\partial u}, \frac{\partial V_{c3}}{\partial u}, \frac{\partial V_{c4}}{\partial u} \right], U_M = \left[\frac{\partial \omega_0}{\partial u}, \frac{\partial \omega_1}{\partial u}, \frac{\partial \omega_2}{\partial u}, \frac{\partial \omega_3}{\partial u}, \frac{\partial \omega_4}{\partial u} \right] \quad (18)$$

The generalized active force is as follows

$$F = U_F[F_0, F_1, F_2, F_3, F_4]^T + U_M[M_0, M_1, M_2, M_3, M_4]^T = U_M[M_0, M_1, M_2, M_3, M_4]^T \quad (19)$$

$$F^* = U_F[F_0^*, F_1^*, F_2^*, F_3^*, F_4^*]^T + U_M[M_0^*, M_1^*, M_2^*, M_3^*, M_4^*]^T \quad (20)$$

The dynamic equation of solar array deployment is expressed as

$$F + F^* = 0 \quad (21)$$

Thus, the dynamic model of solar array deployment can be obtained

$$-m_0 \times \frac{l_0^2}{4} \times \dot{u} - C_A \times (\dot{u} \times \cos^2 \theta - u^2 \times \sin \theta \times \cos \theta) - C_B \times (\dot{u} \times \sin^2 \theta + u^2 \times \sin \theta \times \cos \theta) - (J_0 + J_1 + J_2 + J_3 + J_4) \times \dot{u} - M_q + M_0 + M_1 + M_2 + M_3 + M_4 = 0 \quad (22)$$

where the coefficient C_A and the coefficient C_B represent as follows:

$$C_A = m_1 \times (l_0 + \frac{l_1}{2})^2 + m_2 \times (l_0 + l_1 + \frac{l_2}{2})^2 + m_3 \times (l_0 + l_1 + l_2 + \frac{l_3}{2})^2 + m_4 \times (l_0 + l_1 + l_2 + l_3 + \frac{l_4}{2})^2 \quad (23)$$

$$C_B = m_1 \times (\frac{l_1}{2} - l_0)^2 + m_2 \times (l_1 - l_0 - \frac{l_2}{2})^2 + m_3 \times (l_1 - l_0 - l_2 - \frac{l_3}{2})^2 + m_4 \times (l_1 - l_0 - l_2 - l_3 - \frac{l_4}{2})^2 \quad (24)$$

4.4. Analysis Results

According to the Kane method’s dynamic model, the classical fourth-order Runge–Kutta method is used to solve the numerical problem. The numerical solution of the kinematics and dynamics parameters of the one-dimensional deployment mechanism of the solar array is obtained by programming in MATLAB. The input parameters used are shown in Table 3.

Table 3. Dynamic simulation parameters of the deployment mechanism of the solar array.

S/N	Parameter Name	Symbol	Unit	Value
1	Length of yoke	l_0	m	3.01
2	Length of solar panel	$l_i, (i=1,2,3)$	m	4.05
3	Weight of yoke	m_0	kg	4.3
4	Weight of solar panel	$m_i, (i=1,2,3)$	kg	20
5	Driving torque	M_0	N.m	7.2
6	Driving torque	M_1	N.m	4.3
7	Driving torque	M_2	N.m	4.5
8	Driving torque	M_3	N.m	4.8
9	Driving torque	M_4	N.m	2.5

The Kane method can establish the solar array’s dynamic model and obtain each node’s numerical solution. To verify the correctness of the dynamic model, it is necessary to use the ADAMS method to conduct a real-time simulation analysis of the solar array. When modeling and simulating dynamics with ADAMS, in addition to modeling, defining material properties, and defining motion pairs and driving forces, constraints must be imposed.

Figure 9 shows the change curve of the rotational angle of the root hinge with time during the one-dimensional deployment of the solar array calculated by the Kane method and ADAMS method.

Figure 9 shows the following:

For the one-dimensional deployment direction of a large-scale spatial solar array, the rotational-angle curves of the root hinge calculated by the Kane method and ADAMS are almost the same, which shows the validity and correctness of the Kane method.

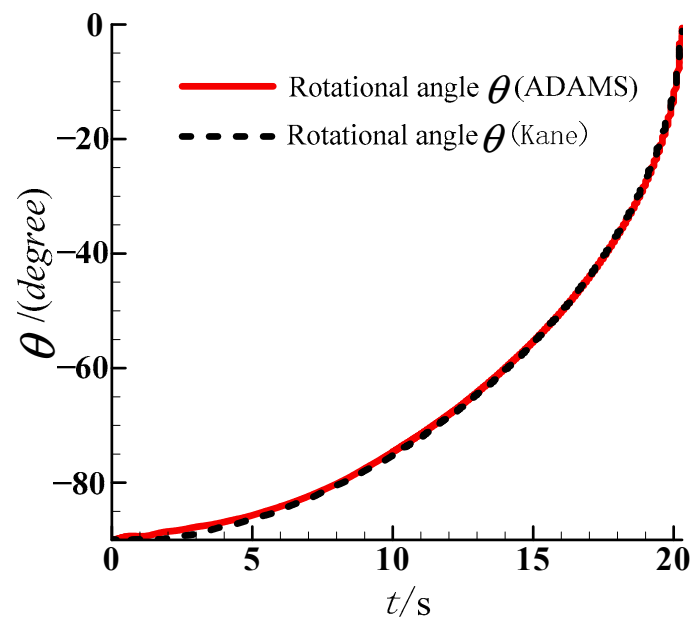


Figure 9. Variation curve of rotational angle of the root hinge θ with time.

5. Deployment Dynamics Simulation of a Large-Scale Spatial Solar Array Based on ADAMS

Based on the abovementioned dynamic modeling, the deployment dynamics analysis and simulation of a two-dimensional large space solar array were performed using ADAMS, and the deployment mechanism with an active speed-limit driving mechanism and traditional damper was dynamically analyzed. The geometric position, velocity, acceleration and other dynamic performances of the deployment process were analyzed, and the deceleration and buffering effects were compared.

5.1. Establishment of Motion Model and Analysis of the Deployment Process for Solar Array

The deployment dynamics model established by ADAMS is shown in Figure 10, divided into the two working conditions of the integrated viscous damper and the combined active speed-limit driving mechanism. The deployment dynamics model of the solar array is established and analyzed in ADAMS. The two-dimensional deployment process is realized through simulation analysis, and the locking impact is obtained.

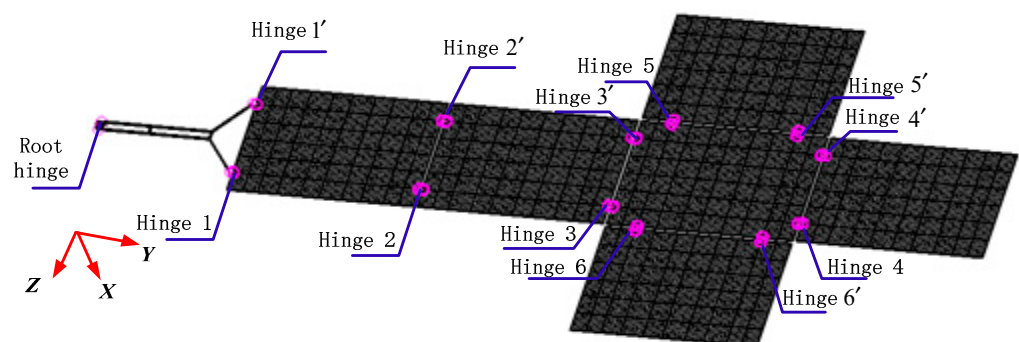


Figure 10. Deployment dynamics model established by ADAMS.

5.2. Deployment Dynamics Analysis of Deceleration of a Root Integrated Viscous Damper

The established dynamic analysis model is used for calculations. The curve of the angular velocity of the yoke with time under this working condition is shown in Figure 11. The angular velocity of the yoke at the end of deployment is $24.7^\circ/\text{s}$. The time history of the Z-direction and Y-direction restraining torque exerted by the solar array on SADA is shown in Figure 12. The maximum Z-direction bending torque produced by the solar array

on SADA during the deployment and locking process is 164.6 N.m, and the Y-direction torsional torque is 143.2 N.m. The force on the damper during the deployment and locking process of the solar array is illustrated in Figure 13, and the maximum torque on the damper is 44.8 N.m.

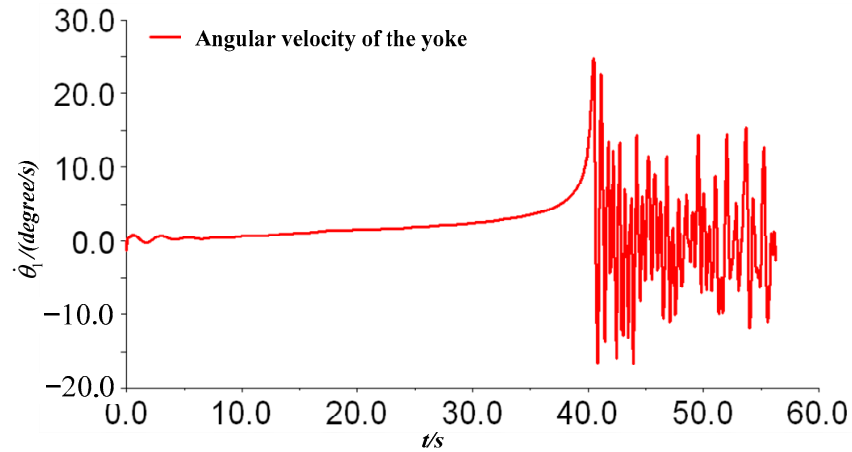


Figure 11. Time varying curve of angular velocity of the yoke.

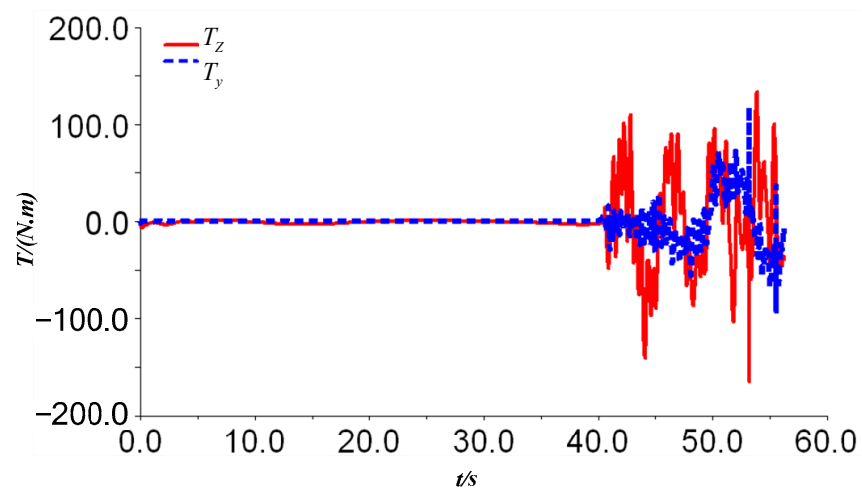


Figure 12. Time history of the torque of the solar array on SADA during the deployment and locking process.

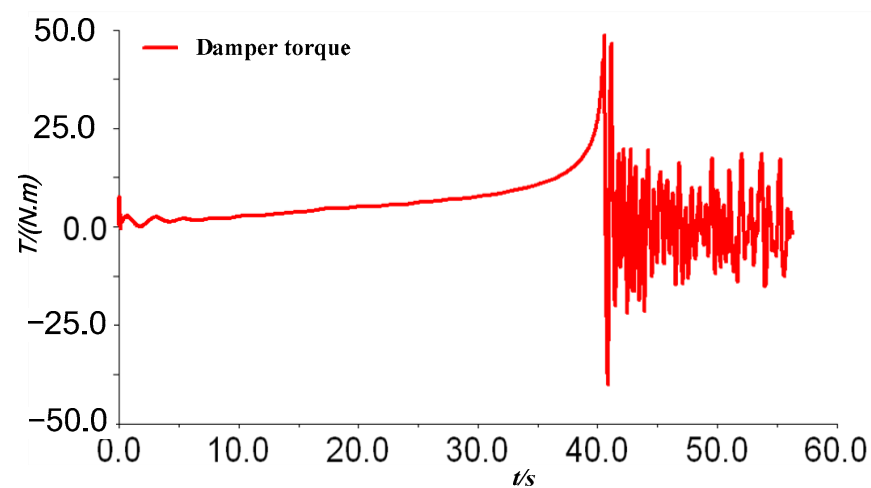


Figure 13. Time varying curve of damper torque during the deployment and locking process.

5.3. Deployment Dynamics Analysis of an Integrated Active Speed-Limit Driving Mechanism

The established dynamic analysis model is used for calculations. The curve of the angular velocity of the yoke with time under this working condition is shown in Figure 14. The angular velocity of the yoke at the end of deployment is $7.8^\circ/\text{s}$. The angular velocity curve of root hinge rotation is shown in Figure 15. SADA is near the root hinge. The time history of the Z-direction and Y-direction restraining torque exerted by the solar array on SADA is illustrated in Figure 16. The maximum Z-direction bending torque generated by the solar array on SADA during the deployment and locking process is $98.2\text{ N}\cdot\text{m}$, and the Y-direction torsional torque is $123.7\text{ N}\cdot\text{m}$. The force on the active speed-limit driving mechanism during deployment and locking of the solar array is shown in Figure 17, and the maximum torque is $96.8\text{ N}\cdot\text{m}$.

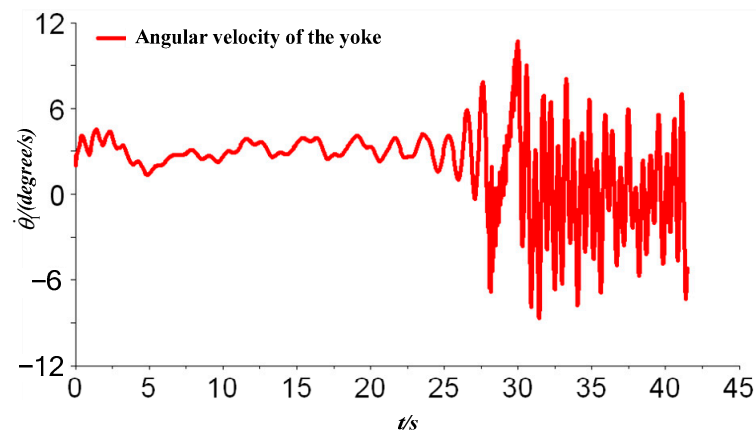


Figure 14. Time varying curve of the angular velocity of the yoke.

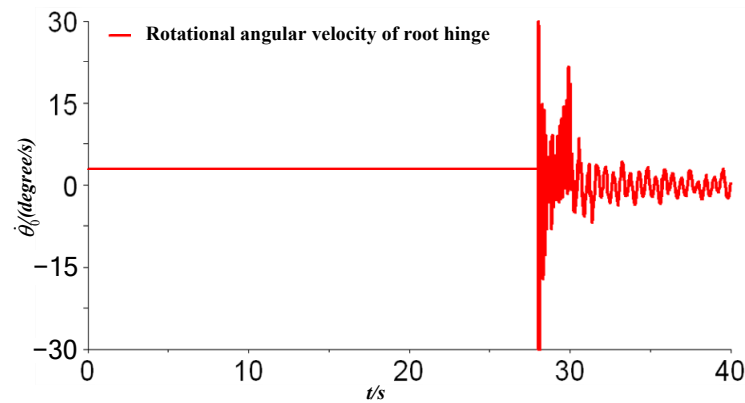


Figure 15. Time varying curve of rotational angular velocity of root hinge.

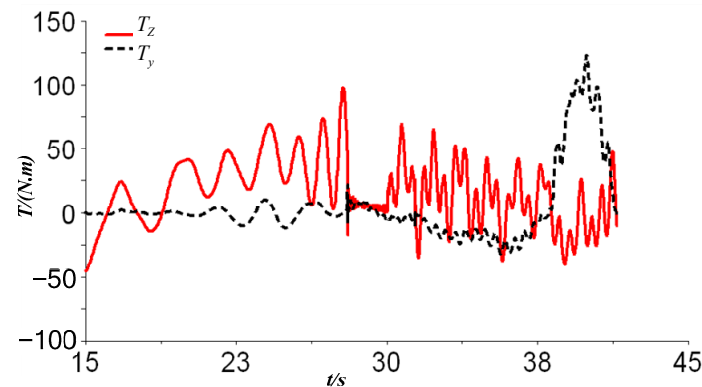


Figure 16. Time history of the torque of the solar array on SADA during the deployment and locking process.

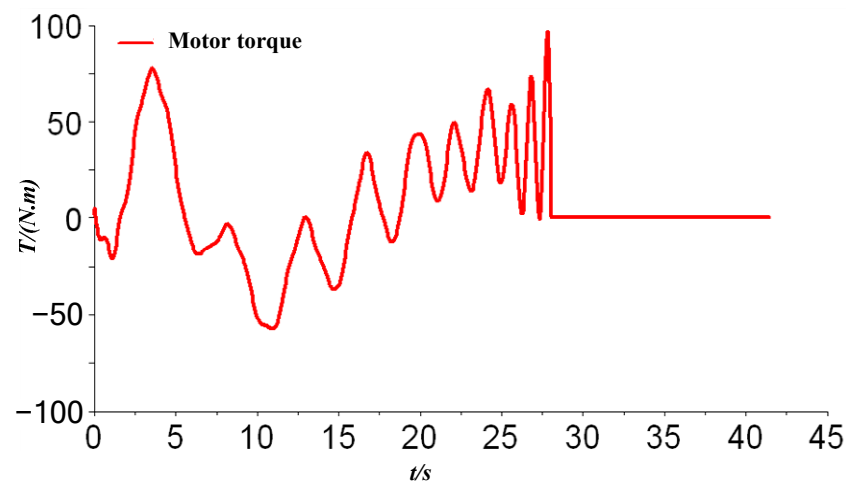


Figure 17. Time varying curve of motor torque during the deployment and locking process.

5.4. Comparative Analysis

The results are summarized in Table 4.

Table 4. Summary of calculation results.

Working Condition	Angular Velocity Before Locking/(rad/s)	Maximum Impact Bending Moment/(N.m)	Maximum Force Moment/(N.m)
Working Condition of Viscous Damper	24.7	164.6	44.8
Working Condition of Active Speed Limiter	7.8	98.2	96.8

The analysis results and Table 4 show the following:

- (1) Damper deceleration is passive, and its deceleration capacity is affected by the capacity of the damper itself, such as volume and weight. The maximum torque that a typical viscous damper can bear is 35 N.m, which can no longer meet the requirement of 44.8 N.m for large-scale two-dimensional deployment solar arrays;
- (2) The active speed-limit driving mechanism can control the deployment speed of the deployment mechanism in real-time and can be adaptively designed according to different deployment configurations and areas;
- (3) Compared with the damper condition, the active speed-limit driving mechanism can reduce the deployment time by 26%; the locking angular speed is reduced by 68%; and the maximum impact bending moment to SADA decreases by 41%;
- (4) Through the analysis of the condition of the active speed-limit driving mechanism, the speed-limiting mechanism is only installed on the root hinge. Thus, the angular velocity change of each component is different during the deployment of the solar array, the synchronous mechanism is required to connect the entire solar array in series, and the stiffness of the synchronous mechanism should be reasonably selected to reduce the instability of the whole system;
- (5) Comparing the two kinds of schemes, the initial velocities of the upper and lower side panels are different due to the large end velocity when the viscous damper is used. The locking time of the two panels is inconsistent, and the locking impact torque of the side panels is large. However, the end speed of the active speed-limit driving mechanism is relatively slow. The locking times of the upper and lower side panels are similar; thus, the locking impact torque is small.

Conclusion: The root hinge with the active speed-limit driving mechanism can achieve the stability of the deployment process of the solar wing and effectively reduce the impact at the moment of deployment and locking. Compared with the traditional viscous damper, it has more significant advantages.

6. Conclusions

This study uses the traditional hinge deployment mode to study the problems of large space solar arrays, such as significant locking impact and unstable movement process. A deployment system of a large-scale spatial solar array that comprehensively uses an active speed-limit driving mechanism and passive spring deployment mechanism is proposed. The main conclusions are as follows:

- (1) A detailed design of the active speed-limit driving mechanism is performed. The drive mode of brushless DC motor + spur gear reduction + torque limiter + planetary reduction + harmonic reduction is adopted to solve the impact of the locking impact of the large solar array on the satellite or the SADA or driving mechanism;
- (2) An adaptive torque limiter suitable for the active speed-limit driving mechanism is designed to solve the possibility that excessive load will damage the active speed-limit driving mechanism during solar array deployment. The spur gear reducer and steel-ball torque limiter in the transmission mechanism are integrated to reduce the volume of the mechanism and simplify the design;
- (3) The Kane method and ADAMS are used to model and simulate the deployment dynamics of a large-scale spatial solar array based on the active speed-limit driving mechanism. The motion and control law of the deployment mechanism of the solar array are obtained. The driving torque, driving mode, driving speed and other dynamic characteristic parameters of the active speed-limit driving mechanism are determined, which can be used to guide the engineering design of the active speed-limit driving mechanism;
- (4) Compared with a viscous damper, the active speed-limit driving mechanism can reduce the deployment time by 26%; the locking angular speed is reduced by 68%; the maximum impact bending moment to SADA is reduced by 41%. The active speed-limit driving mechanism designed in this study can significantly reduce the deployment impact load and increase the deployment reliability.

Author Contributions: Conceptualization, S.Y. and L.S.; methodology, L.L.; software, M.L.; validation, S.Y. and L.L.; formal analysis, S.Y.; investigation, M.L.; resources, L.L.; data curation, S.Y.; writing—original draft preparation, S.Y.; writing—review and editing, L.S.; visualization, S.Y.; supervision, L.S.; project administration, S.Y., L.L. and Y.C.; funding acquisition, Y.C. All authors have read and agreed to the published version of the manuscript.

Funding: This research was funded by the Doctoral Innovation Fund of Xi'an University of Technology, Grant Number 252072104.

Institutional Review Board Statement: Not applicable.

Informed Consent Statement: Not applicable.

Data Availability Statement: The data are contained within the article.

Conflicts of Interest: The authors declare no conflict of interest.

References

1. Jones, P.A.; Spence, B.R. Spacecraft solar array technology trends. *IEEE Aerosp. Electron. Syst. Mag.* **2011**, *26*, 17–28. [[CrossRef](#)]
2. Zhou, X.T.; Ma, X.F.; Li, H.X. Review of flexible tensioned thin-film deployable antennas. *Chin. Space Sci. Technol.* **2022**, *42*, 77–91.
3. Kwak, M.K.; Ra, W.K.; Yoon, K.J. Viscoelastic strain-energy hinge for solar array deployment. *Smart Struct. Mater.* **1999**, *3674*, 341–351. [[CrossRef](#)]
4. Li, H.; Liu, X.; Guo, S.; Cai, G. Deployment dynamics of large-scale flexible solar arrays. *Proc. Inst. Mech. Eng. Part K J. Multi-Body Dyn.* **2016**, *230*, 147–158. [[CrossRef](#)]
5. Kote, A.; Balaji, K.; Nataraju, B.S.; Aralimatti, V.C. Effect of solar array deployment on spacecraft attitude. *J. Spacecr. Technol.* **2007**, *17*, 1–8.
6. Liu, M.L.; Shi, C.; Guo, H.W.; Ma, X.F.; Liu, R.Q.; Hu, F. Innovative design and optimization of the modular high deployment ratio two-dimensional planar antenna mechanism. *Mech. Mach. Theory* **2022**, *174*, 104928. [[CrossRef](#)]
7. Choi, H.S.; Kim, D.Y.; Park, J.H.; Lim, J.H.; Jang, T.S. Modeling and validation of a passive Truss-Link mechanism for deployable structures considering friction compensation with response surface methods. *Appl. Sci.* **2022**, *12*, 451. [[CrossRef](#)]

8. Pyeon, B.D.; Kim, J.H.; Bae, J.S. A study on frequency characteristics of structural hinge stiffness. *J. Vib. Eng. Technol.* **2021**, *9*, 247–255. [[CrossRef](#)]
9. Wu, H.C.; Wang, C.J.; Liu, P. Reliability analysis of deployment mechanism of solar arrays. *Appl. Mech. Mater.* **2011**, *42*, 139–142. [[CrossRef](#)]
10. Liu, Z.Q.; Wu, Y.M.; Ma, J.Y. Design and verification of high-stiffness solar wing on agile satellites. *J. Astronaut.* **2019**, *40*, 621–627.
11. Pu, H.L.; Wang, X.; Yang, Q.L. Analysis of viscous damper effect on solar array deployment. *Spacecr. Eng.* **2013**, *22*, 54–59.
12. Wen, M.F.; Yu, M.; Fu, J.; Wu, Z.Z. Multi-functional hinge equipped with a magneto-rheological rotary damper for solar array deployment system. In Proceedings of the 9th International Symposium on Precision Engineering Measurements and Instrumentation, Changsha/Zhangjiajie, China, 6 March 2015; Volume 9446, pp. 1048–1057.
13. Balaji, K.; Kumar, H.; Nataraju, B.S. Parametric studies on damper for solar array deployment mechanism. *J. Spacecr. Technol.* **2007**, *17*, 9–15.
14. Ahmad, S.S.; Tom, L.; La Rocca, A.; La Rocca, S.; Vakil, G.; Gerada, C.; Benarous, M. Torque limiters for aerospace actuator application. *Energies* **2022**, *15*, 1467. [[CrossRef](#)]
15. Seriani, S.; Gallina, P.; Scalera, L.; Gasparetto, A.; Wedler, A. A new mechanism for the deployment of modular solar arrays: Kinematic and static analysis. In *16th International Symposium on Advances in Robot Kinematics*; Springer International Publishing: Berlin/Heidelberg, Germany, 2019; Volume 8, pp. 372–379.
16. Ding, X.L.; Li, X. Design and test analysis of a solar array root hinge drive assembly. *Chin. J. Mech. Eng.* **2014**, *27*, 909–918. [[CrossRef](#)]
17. Ding, X.L.; Li, X.; Xu, K.; Yang, Q.L.; Pu, H.L. Study on the behavior of solar array deployment with root hinge drive assembly. *Chin. J. Aeronaut.* **2012**, *25*, 276–284. [[CrossRef](#)]
18. Tian, Y.P.; Yang, Y.; Tao, L.; Zhang, X.Y. A novel deployable array mechanism with Two-Dimensional expanding applied to SAR antenna. In Proceedings of the 2016 IEEE International Conference on Information and Automation (ICIA), Ningbo, China, 1–3 August 2016; pp. 391–397.
19. Guo, Y.Z.; Cai, Y.R.; Pan, B.; Gao, F.; Sun, F.X. Two dimensional deployable mechanism for satellites. In Proceedings of the 9th IEEE Annual International Conference on Cyber Technology in Automation, Control, and Intelligent Systems, Suzhou, China, 29 July–2 August 2019; pp. 1079–1084.
20. Wang, Y.S.; Schmitz, A.; Kobayashi, K.; Lopez, J.; Wang, W.; Matsuo, Y.; Sakamoto, Y.; Sugano, S. Exploiting the slip behavior of friction based clutches for safer adjustable torque limiters. In Proceedings of the IEEE International Conference on Advanced Intelligent Mechatronics, Munich, Germany, 3–7 July 2017; pp. 1346–1351.
21. Atallah, K.; Calverley, S.D.; Howe, D. A brushless permanent magnet motor with integrated Torque-Limiter. *IEEE Trans. Magn.* **2007**, *43*, 2498–2500. [[CrossRef](#)]
22. Lai, P.S.; Yang, I.C.; Juan, Y.L.; Chen, T.R.; Chen, C.M. Study on mechanical mechanics and automation with the system analysis and design of the torque limiter functionalities. *Adv. Mater. Res.* **2013**, *703*, 295–299. [[CrossRef](#)]
23. Mohamed, K.; Elgamal, H.; Elsharkawy, A. Dynamic analysis with optimum trajectory planning of multiple degree-of-freedom surgical micro-robot. *Alex. Eng. J.* **2018**, *57*, 4103–4112. [[CrossRef](#)]
24. Elshabasy, M.; Mohamed, K.T.; Ata, A.A. Power optimization of planar redundant manipulator moving along constrained-end trajectory using hybrid techniques. *Alex. Eng. J.* **2017**, *56*, 439–447. [[CrossRef](#)]
25. Balaji, K.; Nataraju, B.S.; Sureshakumar, H.N. Matrix approach to deployment dynamics of an n-panel solar array. *Proc. Inst. Mech. Eng. Part K J. Multi-Body Dyn.* **2003**, *217*, 15–27. [[CrossRef](#)]
26. Xu, Y.; Lin, Q.; Wang, X.; Li, L.; Cong, Q.; Pan, B.; Chen, X. Mechanism design and dynamic analysis of a large-scale spatial deployable structure for space mission. In Proceedings of the 7th International Conference on Electronics and Information Engineering, Nanjing, China, 23 January 2017.
27. Li, H.; Liu, X.; Duan, L.; Cai, G. Deployment and control of spacecraft solar array considering joint stick-slip friction. *Aerosp. Sci. Technol.* **2015**, *42*, 342–352. [[CrossRef](#)]
28. Kwak, M.K.; Heo, S.; Kim, H.B. Dynamics of satellite with deployable rigid solar arrays. *Multibody Syst. Dyn.* **2008**, *20*, 271–286. [[CrossRef](#)]

Disclaimer/Publisher’s Note: The statements, opinions and data contained in all publications are solely those of the individual author(s) and contributor(s) and not of MDPI and/or the editor(s). MDPI and/or the editor(s) disclaim responsibility for any injury to people or property resulting from any ideas, methods, instructions or products referred to in the content.